Ruddlesden-Popper phases as thermoelectric oxides: Nb-doped $SrO(SrTiO_3)_n$ (n=1,2)

Kyu Hyoung Lee
CREST-Japan Science and Technology Agency, 4-1-8 Honcho, Kawaguchi 332-0012, Japan

Sung Wng Kim
Frontier Collaborative Research Center, Tokyo Institute of Technology, 4259 Nagatsuta, Midori, Yokohama 226-8503, Japan

Hiromichi Ohta and Kunihito Koumoto[a)]
Graduate School of Engineering, Nagoya University, Nagoya 464-8603, Japan and CREST-Japan Science and Technology Agency, 4-1-8 Honcho, Kawaguchi 332-0012, Japan

(Received 20 May 2006; accepted 24 June 2006; published online 28 September 2006)

A class of materials known as superlattices has shown substantial promise for potential thermoelectric (TE) applications because of its low thermal conductivity. We have investigated natural superlattice Ruddlesden-Popper (RP) phases [S. N. Ruddlesden and P. Popper, Acta Crystallogr. **10**, 538 (1957)] to elucidate their potential as TE materials. The TE properties of Nb-doped $SrO(SrTiO_3)_n$ (n=1,2) with a RP structure were measured, and the origin of the TE properties is discussed from the viewpoint of the structure of the TiO_6 octahedron. Compared with the cubic perovskite-type Nb-doped $SrTiO_3$, the lattice thermal conductivity decreased by more than 50% (4.4–5 W m^{-1} K^{-1}) at room temperature and by 30% (1.9–2.2 W m^{-1} K^{-1}) at 1000 K. There was a decrease in electrical conductivity owing to the randomly distributed insulating SrO layers in polycrystalline RP phases, and it was found that large TE power can be obtained in conjunction with high symmetry TiO_6 octahedra. The largest dimensionless figure of merit (ZT), 0.14 at 1000 K, was obtained in 5 at. % Nb-doped $SrO(SrTiO_3)_2$. © *2006 American Institute of Physics*.
[DOI: 10.1063/1.2349559]

INTRODUCTION

Perovskites and related compounds can be synthesized with an extremely wide variety of combinations of chemical elements for the following reasons: the perovskite structure accommodates both large (A-site) and small (B-site) cations and provides flexibility for incorporating cations of different sizes as well as a large tolerance for defects (e.g., oxygen deficiency). These enable the perovskite-type oxides to exhibit a number of attractive properties such as optical,[1,2] ferroelectric,[3,4] piezoelectric,[4] magnetic,[5] catalytic,[6] ionically conducting,[7] and thermoelectric (TE) properties.[8–12]

In the field of TE applications, cubic perovskite-type Nb-doped $SrTiO_3$ has been found to exhibit the largest TE performance among n-type oxides ever reported.[8,10] The TE performance, representing the energy conversion efficiency of TE materials, is usually evaluated in terms of a dimensionless figure of merit, $ZT=S^2\sigma T/\kappa$, where Z, T, S, σ, and κ are the figure of merit, the absolute temperature, the Seebeck coefficient, the electrical conductivity, and the thermal conductivity, respectively. The total thermal conductivity (κ_{tot}) is represented as the sum of electronic (κ_{ele}) and lattice contributions (κ_{lat}).

The maximum ZT value for Nb-doped $SrTiO_3$ has been reported to be 0.37 at 1000 K. This large ZT value can be attributed to its large carrier effective mass (m^*), which is derived from the carrier localization that exists as a result of lattice expansion through doping of Nb, having a larger ionic radius than Ti.[8,9] This fact suggests that Nb-doped $SrTiO_3$ would make a good base material for TE applications. However, the ZT value is still too low compared with state-of-the-art Bi–Te alloys,[13] whose ZT is about 1 at 300 K. The main reason for the low ZT values for $SrTiO_3$ systems has been recognized to be their relatively high κ (κ=12 W m^{-1} K^{-1} at 300 K and 3.1 W m^{-1} K^{-1} at 1000 K),[10] which is attributed to a high κ_{lat}, due to the high phonon frequencies of major constituent oxygen, with its small atomic mass. The κ_{lat} value could be reduced by the structural disorder induced by differences in mass and atomic size (phonon scattering by mass fluctuation and point defects).[14] However, this approach is not effective for metal oxides, since oxygen is a major constituent. Another approach to reduce κ_{lat} is the design of artificial superlattices.[15–17] The key feature of the reduction in κ in superlattices is the large number of interfaces, which reduce the lattice contribution through interface phonon scattering.

We focused on a natural superlattice, the Ruddlesden-Popper (RP) phase, $SrO(SrTiO_3)_n$ (n=integer), as TE materials, which have the possibility of exhibiting low κ in the presence of the $SrO/(SrTiO_3)_n$ superlattice. These oxides also have the potential to maintain the favorable electronic properties of $SrTiO_3$ for TE materials, being built up with a sequence of one SrO layer intercalated between n $SrTiO_3$ perovskite layers.[18] In the present study, we investigated the TE properties of Nb-doped $SrO(SrTiO_3)_n$ and demonstrated the origin of the TE properties from the viewpoint of the

[a)]Electronic mail: koumoto@apchem.nagoya-u.ac.jp

structure of TiO_6 octahedra, in addition to the former insight[8,9] into the structural effect in cubic perovskite-type oxides.

EXPERIMENT

$SrO(SrTi_{1-x}Nb_xO_3)_n$ ($x=0-0.2$, $n=1,2$) powders were prepared through the solid-state reaction method, by use of commercial $SrCO_3$, TiO_2, and Nb_2O_5 powders as starting materials. The powders were weighed in the proper ratios and mixed well in an alumina mortar. The mixture was heated at 1200 °C for 12 h in air twice for decarbonization and homogenization of the final samples. To generate the electron carriers through the reduction of Ti^{4+} to Ti^{3+} by doping of Nb^{5+}, the powder was heated at 1400–1450 °C for 2 h in a carbon crucible under an Ar atmosphere. Then, highly dense polycrystalline ceramic samples were fabricated by conventional hot pressing (36 MPa and 1400–1450 °C for 1 h in an Ar flow) of single phase powders. The structural analysis of hot-pressed specimens was carried out by the powder x-ray diffraction using a diffractometer with Cu $K\alpha$ radiation. Structural parameters obtained from the x-ray diffraction data were refined by the Rietveld method by use of the RIETAN-2000 program.[19] The electrical conductivity σ and carrier concentration n_c were measured with a conventional dc four-probe method with a Au electrode under an Ar atmosphere and van der Pauw configuration under vacuum, respectively. The Seebeck coefficient S was measured at 300–1000 K by a conventional steady state method in an Ar flow. Heat capacity and thermal diffusivity were measured by differential scanning calorimetry and laser-flash method under vacuum, respectively. The thermal conductivity κ was calculated with the use of the values of specific heat capacity, thermal diffusivity, and bulk density (98%–99% relative density).

RESULTS AND DISCUSSION

Structural characterization

Figure 1 shows the schematic structure of $SrO(SrTiO_3)_n$ ($n=1,2$) and TiO_6 octahedra in perovskite layers. For $n=1$, the structure is of the tetragonal K_2NiF_4 type (space group, $I4/mmm$) and can be regarded as the alternative stacking of perovskite $SrTiO_3$ layers and SrO rock-salt-type layers.[20] For $n=2$, the space group is tetragonal $I4/mmm$, and two perovskite layers are interleaved with SrO layers.[21] n is equal to the number of layers of corner-sharing TiO_6 octahedra in each perovskite block. If n is infinity (∞), the compound is cubic perovskite-type $SrTiO_3$ (space group, $Pm\bar{3}m$), where each TiO_6 regular octahedron shares its corner three dimensionally. As shown in Fig. 1(c), there are two different Ti–O bonds in $n=1$ $SrO(SrTiO_3)$: the shorter Ti–O1 in the ab plane and the longer Ti–O2 along the c axis. While $n=2$ $SrO(SrTiO_3)_2$ has three different Ti–O bonds, and the Ti ion is situated slightly above the O1 ions along the c axis. As a result, the Ti–O1 layers are not flat, but a little corrugated.

The x-ray diffraction (XRD) patterns revealed that $SrO(SrTi_{1-x}Nb_xO_3)_n$ ($x=0-0.2$, $n=1,2$) was fabricated. Peaks for other phases were not detected in $n=2$ compositions, while a small amount of the $n=2$ phase was found as a second phase in all $n=1$ samples. This feature corresponds well with the calculations by a combination of atomistic computer simulation and high-resolution electron microscopy, suggesting that $n=2$ is the most stable among the Sr–Ti–O system RP phases.[22]

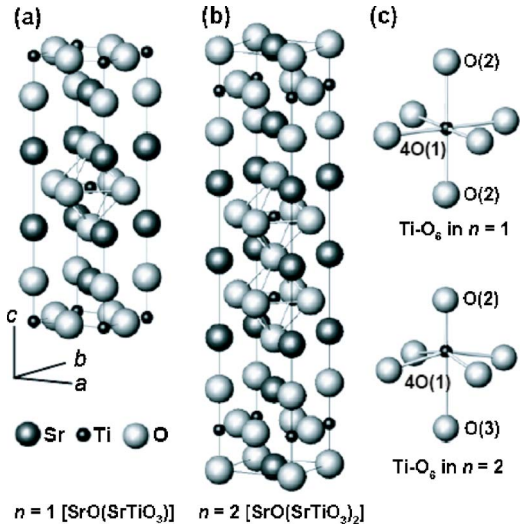

FIG. 1. (Color online) Schematic illustrations of the crystal structure of (a) $SrO(SrTiO_3)_n$ ($n=1$), (b) $SrO(SrTiO_3)_n$ ($n=2$), and (c) TiO_6 octahedra in $n=1$ and $n=2$ phases.

Rietveld refinement for $SrO(SrTi_{1-x}Nb_xO_3)_n$ ($x=0-0.2$, $n=1,2$) was carried out by use of the RIETAN-2000 program.[19] The Rietveld plots of 5 at. % Nb-doped $SrO(SrTiO_3)_n$ ($n=1,2$) are shown in Fig. 2. The reliability factor R_{wp} was 10%–12% in all compounds, and the crystallographic data obtained are given in Tables I and II. The lattice parameters, lattice volumes, and Ti–Ti distance along [110] as functions of Nb content of all compounds are illustrated in Fig. 3. For $n=1$ compounds, the lattice parameter a gradually increases, but the lattice parameter c decreases with increasing Nb content, while for $n=2$, a linearly increases and c increases up to $x=0.1$, becoming constant when x exceeds 0.1. Since the Ti–Ti distance along [110] depends directly on the lattice constant a, the variation of the Ti–Ti distance is similar to that of a for both $n=1$ and 2, and the distance increases with an increase in n. As shown in Fig. 3, the lattice volume (V) increases monotonically with an increase in Nb content both for $n=1$ and 2 compounds. All of these findings can be attributed to the fact that the radius of the Nb^{5+} ion ($r=64$ pm, coordination number=6) is slightly larger than that of Ti^{4+} ion ($r=60.5$ pm, coordination number=6),[23] leading to the lattice expansion in the Nb-doped compounds.

Thermoelectric properties

Figure 4 shows the temperature dependence of the σ for $SrO(SrTi_{1-x}Nb_xO_3)_n$ ($x=0.05-0.2$, $n=1,2$). Those of the cubic perovskite-type 20 at. % Nb-doped $SrTiO_3$ polycrystalline samples are shown for comparison.[10] In the case of $n=1$ and 2, σ increases systematically with increasing amount of Nb doping. Since the doped Nb atom acts as an electron donor, the carrier concentration increases with increasing doping amount, leading to the increase in σ. As shown in

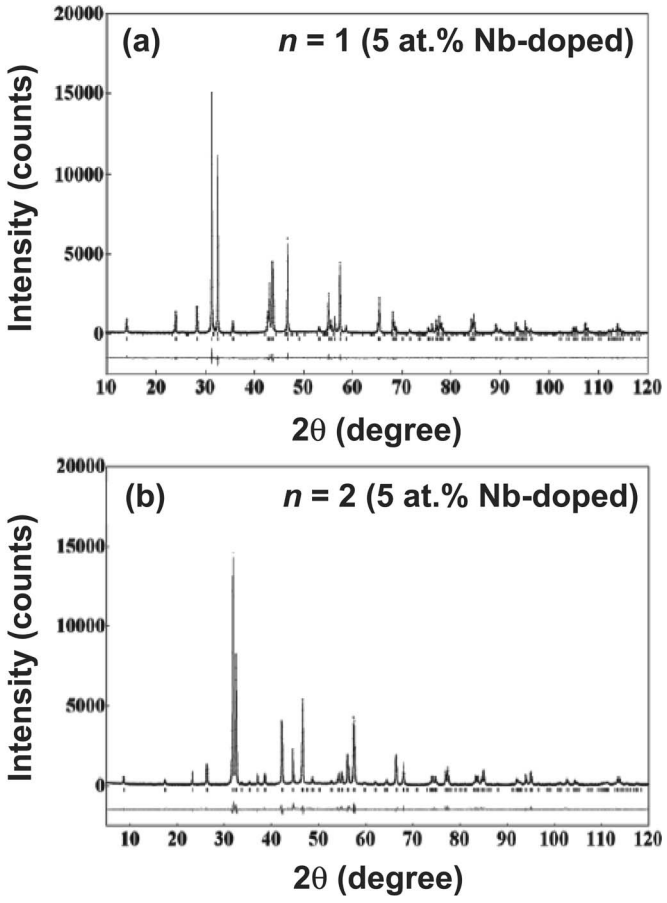

FIG. 2. Rietveld refinement results for (a) 5 at. % Nb-doped $SrO(SrTiO_3)_n$ ($n=1$) and (b) 5 at. % Nb-doped $SrO(SrTiO_3)_n$ ($n=2$). Dots represent the observed data points, the solid line represents a calculated fit to the experiment data, and the bottom line is the difference plot between observed and calculated values.

Fig. 4, σ decreases with temperature proportionally to about $T^{-1.5}$ above ~750 K. The temperature dependence of σ in $SrTiO_3$ systems has already been reported from the viewpoint of Hall mobility (μ).[8,11,12,24,25] The μ value is directly

TABLE I. Crystallographic data for $SrO(SrTi_{1-x}Nb_xO_3)$ ($x=0-0.2$) (SG $I4/mmm$; No. 139).

Atom	Position	x	y	z
Sr	4*e*	0	0	0.3543(7)
				0.3543[a]
				0.3536(9)[b]
				0.3540(3)[c]
Ti	2*a*	0	0	0
O(1)	4*c*	0	0.5	0
O(2)	4*e*	0	0	0.1566(2)
				0.1559(6)[a]
				0.1553(8)[b]
				0.1534(2)[c]
$R_{wp}=0.1011$	$R_I=0.0279$	$R_F=0.0249$	$S=1.52$	
0.1076[a]	0.0234[a]	0.0204[a]	1.73[a]	
0.1181[b]	0.0399[b]	0.0273[b]	1.62[b]	
0.1088[c]	0.0354[c]	0.0256[c]	1.74[c]	

[a] $SrO(SrTi_{0.95}Nb_{0.05}O_3)$.
[b] $SrO(SrTi_{0.9}Nb_{0.1}O_3)$.
[c] $SrO(SrTi_{0.8}Nb_{0.2}O_3)$.

TABLE II. Crystallographic data for $SrO(SrTi_{1-x}Nb_xO_3)_2$ ($x=0-0.2$) (SG $I4/mmm$; No. 139).

Atom	Position	x	y	z
Sr(1)	4*e*	0.5	0.5	0
Sr(2)	2*b*	0.5	0.5	0.1848(4)
				0.1855(6)[a]
				0.1857(3)[b]
				0.1863(7)[c]
Ti	4*e*	0	0	0.0989(3)
				0.0988(8)[a]
				0.0989(9)[b]
				0.0984[c]
O(1)	8*g*	0	0	0.0957(8)
				0.0957(7)[a]
				0.0965(7)[b]
				0.0966(3)[c]
O(2)	4*e*	0	0	0.1909(6)
				0.1908(9)[a]
				0.1899(1)[b]
				0.1860[c]
O(3)	2*a*	0	0.5	0
$R_{wp}=0.1067$	$R_I=0.0291$	$R_F=0.0287$	$S=1.63$	
0.1198[a]	0.0367[a]	0.0292[a]	1.79[a]	
0.1060[b]	0.0232[b]	0.0177[b]	1.66[b]	
0.1104[c]	0.0265[c]	0.0180[c]	1.74[c]	

[a] $SrO(SrTi_{0.95}Nb_{0.05}O_3)_2$.
[b] $SrO(SrTi_{0.9}Nb_{0.1}O_3)_2$.
[c] $SrO(SrTi_{0.8}Nb_{0.2}O_3)_2$.

dependent on the width of the double Schottky barrier (DSB), which can be expressed from Poisson's equation's as[25,26]

$$d_{\mathrm{DSB}} = 2\left(\frac{2\varepsilon_0\varepsilon_r\Phi_B}{eN_D}\right)^{1/2}, \quad (1)$$

where ε_0, ε_r, N_D, and Φ_B are the permittivity of the vacuum, the relative static dielectric constant, the donor density, and the barrier height, respectively. This DSB width becomes small with increasing temperature because ε_r of $SrTiO_3$ decreases proportionally to $T^{-1.5}$, and a power law dependence $\mu \propto T^{-1.5}$ appears at higher temperatures.[25,27] The temperature dependence of σ ($\propto T^{-1.5}$) in Fig. 4 suggests that the electrical conduction in RP phases would take place dominantly within the perovskite layers. The lower σ of RP phases than the perovskite-type ones is considered to be due to the insulating SrO layers randomly distributed in polycrystalline samples.

Figure 5 shows the temperature dependence of S for $SrO(SrTi_{1-x}Nb_xO_3)_n$ ($x=0.05-0.2$, $n=1,2$). The sign of S is negative for all compounds, indicating that the samples are n-type conductors, and the absolute value of S increases proportionally to temperature. The S value decreases with Nb doping owing to an increase in n_c. The Jonker plot at 1000 K is also shown in Fig. 5. The observed slope of the plot is similar to that of cubic perovskite-type La- or Nb-doped $SrTiO_3$ single crystal samples[9] ($-k_B/e \ln 10 = -198\ \mu V\ K^{-1}$). This can be another piece of evidence to support the idea that the electronic transport properties of RP phases are dominated by perovskite layers. The TE properties of $SrO(SrTi_{1-x}Nb_xO_3)_n$ ($x=0.05$, 0.1, $n=1$, 2) inclusive of S are

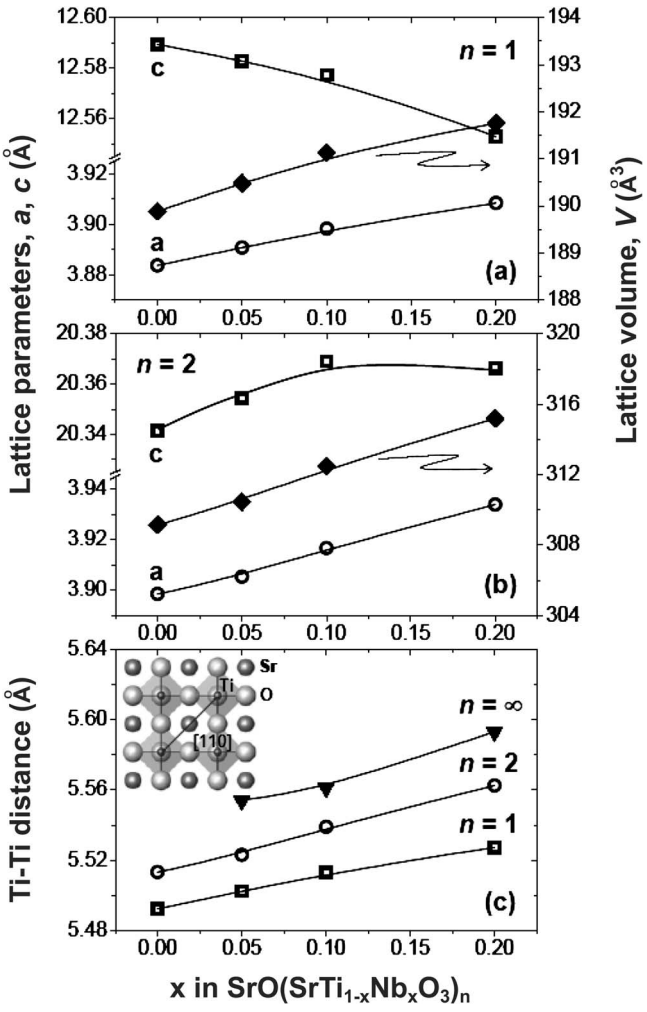

FIG. 3. Variation of lattice parameters with Nb content for (a) $n=1$ and (b) $n=2$ phases and (c) Ti–Ti distance along [110] for $n=1$, 2, and ∞ phases. Data for $n=\infty$ epitaxial film shown in (c) are taken from Ref. 8 (inverted filled triangles).

summarized in Table III. It can be clearly seen in the inset of Fig. 5 and Table III that S values for RP phases are much lower than those of cubic perovskite-type $SrTiO_3$, even at lower n_c. This difference in TE behavior can also be seen in power factor (PF) data. Figure 6 shows the calculated PF values of the Nb-doped $SrO(SrTiO_3)_n$ ($n=1,2$) and the n_c dependence of PF at 1000 K. PF for cubic perovskite-type Nb-doped $SrTiO_3$ increased gradually with n_c, and it became saturated at $n_c \sim 7\times10^{21}$ cm^{-3},[8] but in contrast, the n_c ($\sim 5\times10^{20}$ cm^{-3}) of Nb-doped $SrO(SrTiO_3)_n$ ($n=1,2$) showing the maximum PF is much lower than that of Nb-doped $SrTiO_3$.

To clarify the difference in TE behavior between cubic perovskite-type and RP phases, we calculated the effective mass value m^* and represented them in Fig. 7 and Table III. The m^* was estimated with the use of the following equation:[28]

$$m^* = \frac{h^2}{2k_BT}\left[\frac{n_c}{4\pi F_{1/2}(\xi)}\right]^{2/3}, \tag{2}$$

where h, k_B, F_n, and ξ are the Plank constant, the Boltzmann constant, the Fermi integral, and the chemical potential, respectively. The use of classical statistics in describing the behavior of the carriers is justified only in the limit of low carrier concentration. Because the thermoelectric material has to be doped heavily, Fermi-Dirac statistics should be employed. The Seebeck coefficient and Fermi integral can be expressed as

$$S = -\frac{k_B}{e}\left[\frac{(r+2)F_{r+1}(\xi)}{(r+1)F_r(\xi)} - \xi\right], \tag{3}$$

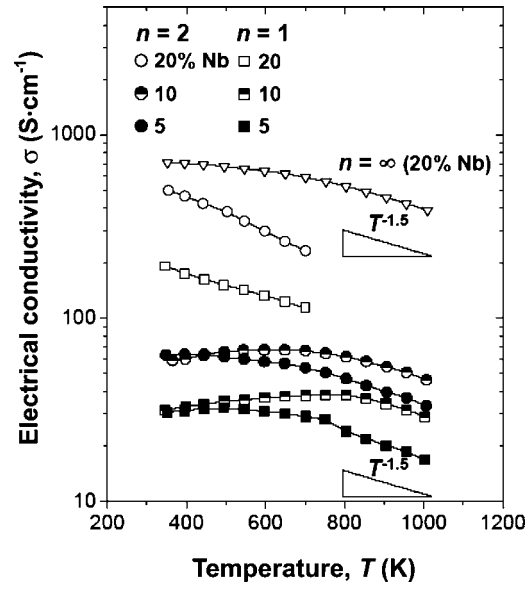

FIG. 4. Temperature dependence of electrical conductivity for $SrO(SrTi_{1-x}Nb_xO_3)_n$ ($n=1,2$). Inverted open triangles represent the data for cubic perovskite-type 20 at. % Nb-doped $SrTiO_3$ ($n=\infty$) polycrystalline samples in Ref. 10.

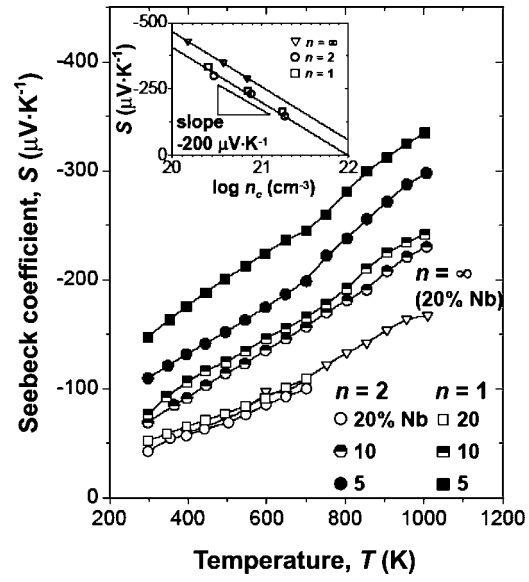

FIG. 5. Temperature dependence of the Seebeck coefficient for $SrO(SrTi_{1-x}Nb_xO_3)_n$ ($n=1,2$). Inverted open triangles represent the data for cubic perovskite-type 20 at. % Nb-doped $SrTiO_3$ perovskite ($n=\infty$) polycrystalline samples in Ref. 10. The Jonker plots of S values for $SrO(SrTi_{1-x}Nb_xO_3)_n$ ($n=1,2$) at 1000 K are shown in the inset. Inverted open triangles represent the data for cubic perovskite-type La- or Nb-doped $SrTiO_3$ single crystal samples in Ref. 9.

TABLE III. Carrier concentration (n_c), electrical conductivity (σ), Hall mobility (μ), Seebeck coefficient (S), and carrier effective mass (m^*) for Nb-doped $SrO(SrTiO_3)_n$ ($n=1,2$) at room temperature.

Compositions	n_c (10^{20} cm^{-3})	σ (S cm^{-1})	μ (cm^2 V^{-1} s^{-1})	S (μV K^{-1})	m^* (m_0)
5 at. % Nb-doped $n=1$	2.5	30	0.8	−147	2.2
10 at. % Nb-doped $n=1$	6.9	30	0.3	−77	2.1
5 at. % Nb-doped $n=2$	2.9	62	1.4	−109	1.8
10 at. % Nb-doped $n=2$	7.5	58	0.5	−69	1.9
Nb-doped single crystal[a]	1.5	95	6.2	−330	7.3
Nb-doped single crystal[a]	3.7	353	6.0	−240	7.7
La-doped single crystal[a]	6.8	1000	9.2	−150	6.6

[a]Reference 9.

$$F_n(\xi) = \int_0^\infty \frac{x^n}{1+e^{x-\xi}} dx, \tag{4}$$

where e is the electronic charge and r is the scattering parameter of relaxation time. There is an anomaly of S at about 750 K, as shown in Fig. 5. We assumed that carriers are scattered only by acoustic phonons above 750 K, and $r=0$,[29] while below 750 K, carriers are scattered by both polar optical phonons and acoustic phonons, and the scattering parameter of relaxation time gradually increases with decreasing temperature, reaching 0.5 at room temperature.

As shown in Fig. 7, m^* increases linearly with increasing Ti–Ti distance in cubic perovskite-type La- or Nb-doped $SrTiO_3$ which have regular TiO_6 octahedra, indicating that m^* could be increased by increasing the Ti–Ti distance (decreasing the overlapping between Ti $3d$-t_{2g} orbitals) if the degenerate band is maintained. This phenomenon allows the large PF in cubic perovskite-type $SrTiO_3$ even at high n_c. However, unfortunately, the TiO_6 octahedra in $SrO(SrTiO_3)_n$ are slightly deformed, as shown in Fig. 1(c). The deformed TiO_6 might have a deleterious effect on the TE properties by leading to variations of the density of states (DOS) such as band splitting, frequently observed in low symmetry (e.g., orthorhombic) structure materials.[30,31] The resulting m^* values are $1.8-2.4m_0$ and show great deviation from the linear relation of cubic perovskite-type $SrTiO_3$. It is considered that small m^* values for RP phases are due to the crystal field splitting of Ti $3d$-t_{2g} orbitals (splitting of degeneracy) by the presence of deformed TiO_6 octahedra and could be responsible for low S. Accordingly, the effect of enlargement of m^* originating from carrier localization as a result of lattice expansion by doping of Nb must be limited to structures with high symmetry TiO_6 octahedra. Barium could be a candidate as a larger A-site substitutional ion in $SrTiO_3$ systems.

Figure 8 shows the temperature dependence of κ for 5 at. % Nb-doped $SrO(SrTiO_3)_n$ ($n=1,2$). The electronic contribution (κ_{ele}) to κ_{tot} can be calculated with the use of the Wiedemann-Franz law expressed by

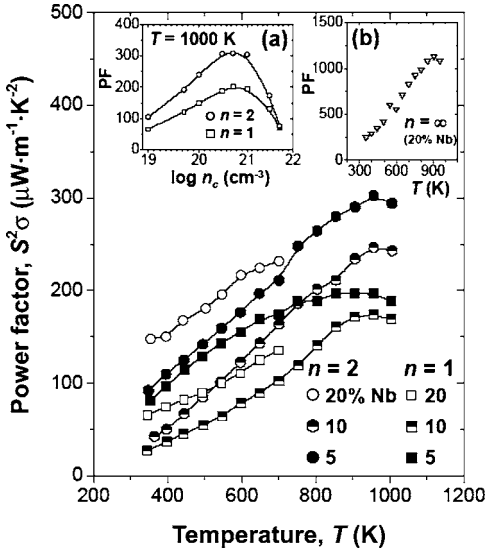

FIG. 6. Temperature dependence of the power factor for $SrO(SrTi_{1-x}Nb_xO_3)_n$ ($n=1,2$). The estimated power factor with carrier concentration is also shown in inset (a). Power factor data for cubic perovskite-type 20 at. % Nb-doped $SrTiO_3$ perovskite ($n=\infty$) polycrystalline samples calculated from the data in Ref. 10 are shown in inset (b).

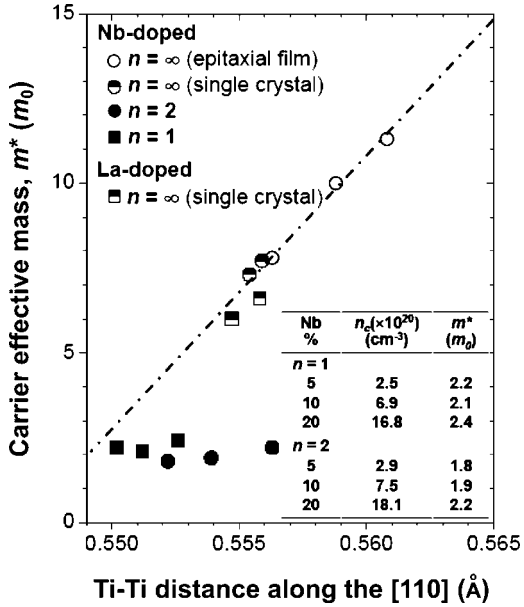

FIG. 7. Carrier effective mass data for RP and perovskite structure phases as a function of Ti–Ti distance. Open circles represent the data for cubic perovskite-type Nb-doped $SrTiO_3$ ($n=\infty$) epitaxial films in Ref. 8, and half-filled circles and half-filled squares represent the data for cubic perovskite-type Nb- and La-doped $SrTiO_3$ ($n=\infty$) single crystals in Ref. 9, respectively. The values of carrier concentration (n_c) and carrier effective mass (m^*) with Nb content are shown in the inset.

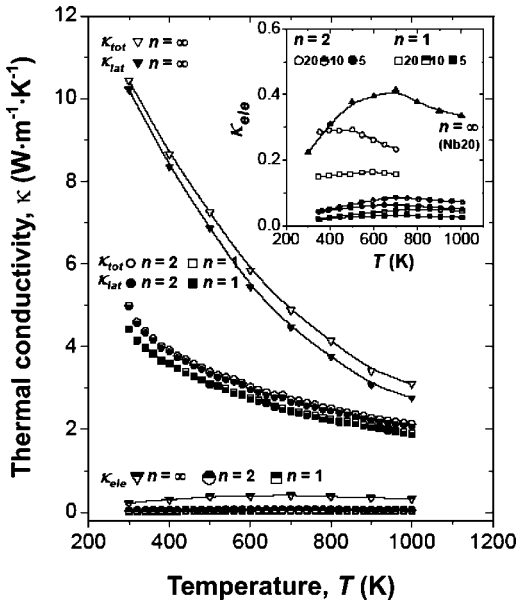

FIG. 8. Temperature dependence of thermal conductivity for 5 at. % Nb-doped $SrO(SrTiO_3)_n$ ($n=1,2$). The thermal conductivity data (open, filled, and half-filled inverted triangles) for cubic perovskite-type 20 at. % Nb-doped $SrTiO_3$ perovskite ($n=\infty$) polycrystalline ceramics are taken or calculated from the data in Ref. 10. Electronic thermal conductivity (κ_{ele}) data with Nb content estimated using the Wiedemann-Franz law are also shown in the inset.

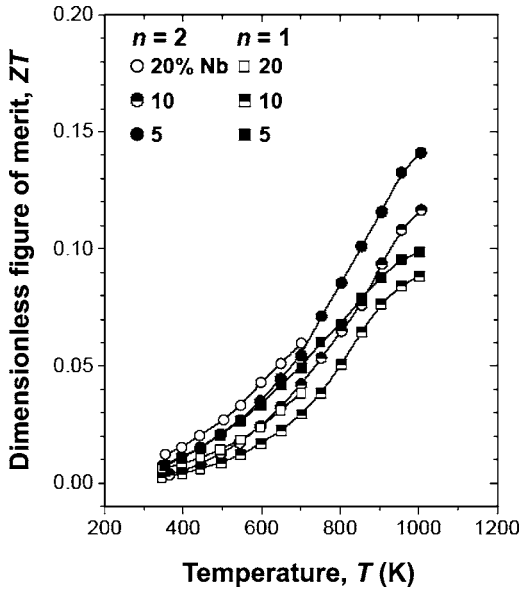

FIG. 9. Dimensionless thermoelectric figures of merit for SrO $(SrTi_{1-x}Nb_xO_3)_n$ ($n=1,2$).

$$\kappa_{ele} = L_0 \sigma T, \tag{5}$$

where L_0 is the Lorenz number. Similar to the Hall coefficient and S, the Lorenz number can be expressed as follows:[28]

$$L_0 = \frac{k_B^2}{e^2}\left[\frac{3F_0(\xi)F_2(\xi) - 4F_1^2(\xi)}{F_0^2(\xi)}\right], \tag{6}$$

where the Fermi integral values were obtained from the measured S with the use of Eqs. (3) and (4). The κ_{ele} was estimated with the use of the calculated L_0 [$(1.5-2.35)\times10^{-8}$ W Ω K^{-2}] and the experimental σ data. Although κ_{ele} increases with increasing Nb content, the κ_{tot} shows no significant dependence on the Nb content because the contribution of κ_{ele} to κ_{tot} is very small ($\kappa_{ele} \sim 0.3$ W m^{-1} K^{-1}). In comparison with the cubic perovskite-type Nb-doped $SrTiO_3$ polycrystalline ceramics, κ_{lat} decreased in value by more than 50% [(4.4–5) W m^{-1} K^{-1}] at room temperature and 30% [(1.9–2.2) W m^{-1} K^{-1}] at 1000 K, respectively. This reduction in the κ value would have been caused by the enhancement of phonon scattering at the $SrO/(SrTiO_3)_n$ internal interfaces.

Figure 9 shows the temperature dependence of the ZT for $SrO(SrTi_{1-x}Nb_xO_3)_n$ ($x=0.05-0.2$, $n=1,2$) phases. The ZT value drastically increases with increasing temperature in all compositions. Overall ZT values of $SrO(SrTi_{1-x}Nb_xO_3)_n$ ($x=0.05$, 0.1, $n=1$, 2) were in the range of 0.09–0.14 at 1000 K, and the largest ZT, 0.14 at 1000 K, was obtained in 5 at. % Nb-doped $SrO(SrTiO_3)_2$. In spite of their low κ, ZT values of Nb-doped $SrO(SrTiO_3)_n$ were lower than that of cubic perovskite-type Nb-doped $SrTiO_3$ (0.37 at 1000 K).[8] As mentioned above, the key reasons for relatively low ZT of RP phases are firstly the low σ caused by the insertion of insulating SrO layers into perovskite structures and secondly the small S (low m^*), possibly caused by splitting of degeneracy due to the deformation of TiO_6 octahedra in perovskite layers. The following points remain to be further clarified in future investigations in order to obtain the maximum TE efficiency in RP phases: the optimum composition to realize high symmetry TiO_6 octahedra in perovskite layers, structural anisotropy in TE properties, and processes for producing textured (crystal-axis-oriented) ceramics and thin films.

SUMMARY

We investigated the phase formation and TE properties of polycrystalline Nb-doped $SrO(SrTiO_3)_n$ natural superlattice Ruddlesden-Popper phases. Single phases of 0–20 at. % Nb-doped $SrO(SrTiO_3)_n$ ($n=2$) were synthesized, while a small amount of $n=2$ phase was found as a second phase in all $n=1$ samples. Although changes in lattice parameters by Nb doping were observed, the symmetry of the deformed TiO_6 octahedra was not largely improved. Because of this low symmetry of TiO_6 octahedra in RP phases, the m^* ($m^*=1.8-2.4m_0$) is much smaller than that of perovskite ($m^*=6-12m_0$). TE properties indicate that the electronic transport properties in RP phases are dominated by the feature of perovskite layers. Large reductions in thermal conductivity of RP phases were clearly observed, compared to cubic perovskite-type $SrTiO_3$, indicating the enhancement of phonon scattering at $SrO/(SrTiO_3)_n$ internal interfaces. Overall ZT values of $SrO(SrTi_{1-x}Nb_xO_3)_n$ ($x=0.05$, 0.1, $n=1$, 2) obtained in the present study were in the range of 0.09–0.14 at 1000 K, and the largest ZT, 0.14 at 1000 K, was observed for 5 at. % Nb-doped $SrO(SrTiO_3)_2$.

ACKNOWLEDGMENTS

The authors would like to thank Dr. Hideki Kita and Dr. Hideki Hyuga of the National Institute of Advanced Indus-

trial Science and Technology (AIST), Japan for their technical assistance in hot pressing. The authors would also like to thank Dr. Kouta Iwasaki (Nagoya University) for a careful discussion on the Rietveld refinement.

[1]F. Jona, G. Shirane, and R. Pepinsky, Phys. Rev. **97**, 1584 (1955).
[2]M. P. Moret, M. A. C. Devillers, K. Wörhoff, and P. K. Larsen, J. Appl. Phys. **92**, 468 (2002).
[3]D. Dimos and C. H. Mueller, Annu. Rev. Mater. Sci. **28**, 397 (1998).
[4]T. M. Shaw, S. Trolier-McKinstry, and P. C. McIntyre, Annu. Rev. Mater. Sci. **30**, 263 (2000).
[5]M. A. Gilleo, J. Chem. Phys. **24**, 1239 (1956).
[6]R. Spinicci, A. Tofanari, A. Delmastro, D. Mazza, and S. Ronchetti, Mater. Chem. Phys. **76**, 20 (2002).
[7]K. Huang, M. Feng, and J. B. Goodenough, J. Electrochem. Soc. **144**, 3620 (1997).
[8]S. Ohta, T. Nomura, H. Otha, M. Hirano, H. Hosono, and K. Koumoto, Appl. Phys. Lett. **87**, 092108 (2005).
[9]S. Ohta, T. Nomura, H. Otha, and K. Koumoto, J. Appl. Phys. **97**, 034106 (2005).
[10]S. Ohta, H. Otha, and K. Koumoto, J. Ceram. Soc. Jpn. **114**, 102 (2006).
[11]R. Moos and K. H. Härdtl, J. Appl. Phys. **80**, 393 (1996).
[12]H. Muta, K. Kurosaki, and S. Yamanaka, J. Alloys Compd. **368**, 22 (2004).
[13]T. M. Tritt, Science **283**, 804 (1999).
[14]L. Tewordt and T. Wölkhausen, Solid State Commun. **70**, 839 (1989).
[15]S. M. Lee, D. G. Cahill, and R. Venkatasubramanian, Appl. Phys. Lett. **70**, 2957 (1997).
[16]W. S. Capinsky, H. J. Maris, T. Ruf, M. Cardona, K. Ploog, and D. S. Katzer, Phys. Rev. B **59**, 8105 (1999).
[17]M. N. Touzelbaev, P. Zhou, R. Venkatasubramanian, and K. E. Goodson, J. Appl. Phys. **90**, 763 (2001).
[18]K. Koumoto, S. Ohta, and H. Ohta, Proceedings of the 23rd International Conference on Thermoelectrics, IEEE, Piscataway, 2005 (unpublished), p. 92.
[19]F. Izumi and T. Ikeda, Mater. Sci. Forum **321**, 198 (2000).
[20]S. N. Ruddlesden and P. Popper, Acta Crystallogr. **10**, 538 (1957).
[21]S. N. Ruddlesden and P. Popper, Acta Crystallogr. **11**, 54 (1958).
[22]A. McCoy, R. W. Grimes, and W. E. Lee, Philos. Mag. A **75**, 833 (1997).
[23]R. D. Shannon, Acta Crystallogr., Sect. A: Cryst. Phys., Diffr., Theor. Gen. Crystallogr. **A32**, 751 (1976).
[24]R. Moos, W. Menesklou, and K. H. Härdtl, Appl. Phys. A: Mater. Sci. Process. **61**, 389 (1995).
[25]S. Ohta, Ph.D. thesis, Nagoya University, 2006.
[26]G. Blatter and F. Greuter, Phys. Rev. B **33**, 3952 (1986).
[27]H. Takashima, R. Wang, M. Okano, A. Shoji, and M. Itoh, Jpn. J. Appl. Phys., Part 2 **43**, L170 (2004).
[28]V. I. Fistul, *Heavily Doped Semiconductors* (Plenum, New York, 1969).
[29]K. Durczewski and M. Ausloos, Phys. Rev. B **61**, 5303 (2000).
[30]T. M. Mishonov, I. N. Gentchev, and R. K. Koleva, Superlattices Microstruct. **24**, 381 (1998).
[31]R. Vidya, P. Ravindran, A. Kjekshus, H. Fjellvag, and B. C. Hauback, J. Solid State Chem. **177**, 146 (2004).